RSC Advances

ROYAL SOCIETY OF CHEMISTRY

PAPER

View Article Online
View Journal | View Issue

Check for updates

Cite this: *RSC Adv.*, 2026, **16**, 24248

$In_2O_3/AgBiS_2$ heterojunction – gated organic photoelectrochemical transistor with DNAzyme-mediated reaction for sensitive detection of bisphenol A

Tingting Zhang, *[ab] Qiyue Tao,[a] Jiahe Chen,[b] Jia-Hao Chen,*[b] Hong Zhou [b] and Zhijie Zhang[a]

Received 26th March 2026
Accepted 30th April 2026

DOI: 10.1039/d6ra02509a

rsc.li/rsc-advances

In recent years, organic photoelectrochemical transistor (OPECT) sensors have attracted growing attention in various fields. Nevertheless, their potential remains far from being fully exploited, and these systems still face substantial challenges. In this work, a novel OPECT aptamer biosensor is rationally designed and fabricated by integrating photoelectrochemical analysis with organic electrochemical transistor technology. In this sensor, $In_2O_3/AgBiS_2$ is employed as the photoactive material, and target-specific DNA strand displacement hybridization is utilized as the signal amplification strategy. Specifically, for bisphenol A (BPA) detection, DNAzyme (G-quadruplex/hemin) acts as a horseradish peroxidase (HRP) mimic to catalyze H_2O_2-mediated oxidation reactions, generating insoluble precipitation, which markedly decreases ΔI_{DS}. Experimental verification shows that the developed sensor exhibits excellent analytical performance. Its linear detection range can cover from 1 fg mL^{-1} to 0.1 ng mL^{-1}, and the limit of detection is as low as 0.29 fg mL^{-1}. This innovative biosensing platform not only provides a highly potential solution for the accurate detection of BPA but also shows broad application prospects and great development potential in the future expansion of the analysis and detection of other pollutants.

Introduction

Bisphenol A (BPA, 2,2-bis(4-hydroxyphenyl)propane) is a widely used plastic monomer and industrial reagent employed in the synthesis of polycarbonate plastics and epoxy resins, which are commonly used in food and beverage containers, packaging, infant bottles, and dental sealants.[1–4] Trace amounts of BPA can migrate from these materials into food and beverages and this process is temperature-dependent and can be exacerbated by heating and washing, leading to human exposure *via* ingestion.[5] BPA is an endocrine-disrupting chemical that acts by mimicking estrogen, thereby interfering with hormone-regulated pathways related to growth, development, and reproduction.[6] Prolonged exposure has been epidemiologically associated with a range of adverse health outcomes, including birth defects, infertility, precocity, obesity, elevated risks of mammary and prostate cancer, as well as increased incidence of cardiovascular disease and diabetes.[7–10] The discharge of BPA-containing wastewater into seawater exposes aquatic organisms and humans to high levels of BPA, thus posing a serious threat to human health.[11] Therefore, the development of rapid, sensitive, and convenient analytical methods for BPA detection is of great importance for environmental protection, risk assessment, and the safeguarding of food safety and public health.

Photoelectrochemical (PEC) biosensing technology, as an important branch in the field of cutting-edge analysis, has demonstrated unique theoretical advantages and application potentials in recent years.[12,13] However,the inherently low signal amplification ability of traditional PEC sensing fundamentally limits its detection performance.[14,15] Organic electrochemical transistor (OECT) has become a breakthrough technology platform in the field of bioelectronics by virtue of its unique bulk ion modulation mechanism, and has demonstrated significant advantages in applications such as biosensing and neural interfaces.[16,17] Compared to conventional transistor devices, OECTs achieve excellent transconductance performance and signal amplification through the diffusion and doping process of ions in the organic semiconductor bulk phase, which provides an ideal solution for the detection of weak electrical signals (*e.g.*, neuronal action potentials).[18–20] However, typical OECT devices based on the poly(3,4-ethylenedioxythiophene):poly (styrene sulfonate) (PEDOT:PSS)

---

[a] *Jiangsu Provincial Key Laboratory for Chemistry of Low-Dimensional Materials, School of Chemistry and Chemical Engineering, Huaiyin Normal University, Huai'an, 223300, Jiangsu, China. E-mail: tingtingzhang@hytc.edu.cn*

[b] *Key Laboratory of Optic-Electric Sensing and Analytical Chemistry for Life Science, MOE, College of Chemistry and Molecular Engineering, Qingdao University of Science and Technology, Qingdao, 266042, People's Republic of China. E-mail: cjh807757290@126.com*

system face a non-negligible problem of background interference during long-term operation – the inherent redox properties of this conductive polymer coupled with the interfacial coupling effect of the bio-detecting system lead to device significant fluctuations in baseline current.[21,22] How to synergistically suppress the background signal at the level of intrinsic material properties and device architecture while maintaining excellent transconductance performance has become a key scientific issue to drive OECT towards ultrasensitive biosensing applications. It is noteworthy that the cross-study of light-controlled OECT is driving the field into a new dimension – the breakthrough advantage of organic photoelectrochemical transistors (OPECTs) in ultra-low background detection by precisely tuning the light-semiconductor-OECT ternary interfacial interactions.[23–27] The design of the signal amplification mechanisms and the gate plays important role in OPECT performance.

In_2O_3 is a typical n-type semiconductor with a band gap of 2.6–2.8 eV.[28,29] It demonstrates good electrical conductivity along with effective charge transfer capability.[30,31] However, In_2O_3 suffers from low optical energy utilization efficiency and high carriers-recombination rate.[32,33] One of the promising methods to improve the performance of In_2O_3 is to form heterojunctions with other materials.[34–36] The ternary chalcogenide compound $AgBiS_2$ is highly photoactive and has excellent performance in photocatalysis, solar cells, photodetectors, and photothermal converters.[37] $AgBiS_2$ has a band gap of *ca.* 1.2 eV, which could form a band gap-matched type-II heterojunction with In_2O_3.[38] Therefore, the type-II $In_2O_3/AgBiS_2$ heterostuctures are expected to significantly facilitate the separation and transport of photogenerated charges.[39]

The soluble 4-chloro-1-naphthol (4-CN) can be converted into insoluble benzo-4-chlorohexadienone (4-CD) precipitation in the presence of H_2O_2 and horseradish peroxidase (HRP).[40,41] Liu and co-workers constructed a dual-enzyme cascade horseradish peroxidase (HRP)@glucose oxidase (GOx)/Pt/n-Si-gated OPECT system with poly(3,4-ethylenedioxythio-phene):poly(styrene sulfonate) (PEDOT:PSS) as the channel, which realizes glucose detection.[24] 4-CD precipitation produced on the gate can impede the light transmission of Pt film and hinder the electron transport at the interface of electrode/electrolyte, which leads to a vital decrease in ΔI_{DS}. However, the native HRP is prone to degradation due to its sensitivity to environmental factors.[42,43] Nowadays, numerous HRP mimic enzymes have been developed to overcome the instability of natural enzymes, among which the G-rich DNA/Hemin-based DNAzyme (G-quadruplex/hemin) exhibits significant HRP activity.[44] Given that G-rich DNA is a guanine-rich DNA sequence, hybridization chain reaction (HCR) can be employed to amplify DNA fragments, which could increase the quantity of G-quadruplex/hemin assemblies and enhance their corresponding enzymatic activity.[45,46]

In this work, we report a sensitive OPECT system for BPA detection based on poly(3,4-ethylenedioxythiophene):poly (styrene sulfonate) (PEDOT:PSS) and $In_2O_3/AgBiS_2$ heterojunction as the photoactive materials (Scheme 1). The preparation process of $In_2O_3/AgBiS_2$ heterojunction (Scheme 1A) is shown in detail, where the two single materials are prepared separately by hydrothermal method, and then the heterojunction is formed by ultrasonication to produce electrostatic adsorption of the two materials. The preparation process of this system for sensing and the specific configuration of the organic photoelectrochemical transistor was depicted in Scheme 1B and Scheme 1C. The $In_2O_3/AgBiS_2$ heterojunction was modified on the gate electrode, which can facilitate the separation and transport of photogenerated charges. Then, the aptamer-cDNA hybrid duplex was immobilized on gate electrode sequentially, which serves as a recognition unit for BPA detection. The aptamer binds to BPA and dissociates from the electrode surface in the present of BPA.[47–50] Hybridization chain reaction is triggered by the released cDNA as an initiator DNA in the presence of two hairpin DNA strands (H1 and H2) and many G-rich sequences can be produced. After the addition of Hemin, DNAzyme is formed acted as mimic HPR. A large amount of 4-CD recipitation forms and is deposited onto the electrode surface, which hinders the electron transport at the interface of electrode/electrolyte and results in a decrease of ΔI_{DS}. Based on the construction of $In_2O_3/AgBiS_2$ gate and the hybridization chain reaction, it is expected to realize the precise regulation of light–matter interactions in OPECT devices by taking advantage of the synergistic effect of their photoresponse cascade amplification effect and directional charge transport channels. The OPECT detection system achieves the high sensitivity for BPA detection with the linear detection range of 1 fg mL^{-1} to 0.1 ng mL^{-1} and detection limit of 0.29 fg mL^{-1}, which provides a functional OPECT platform for the detection of BPA and other marine pollutants.

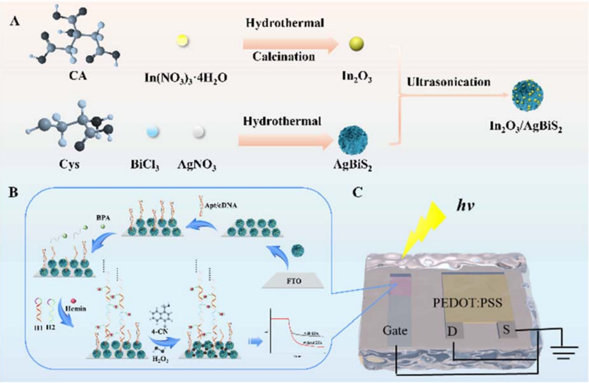

Scheme 1 (A) Preparation of $In_2O_3/AgBiS_2$ heterojunction. (B) The fabrication process and the operating mechanism of OPECT system for BPA. (C) Schematic of the OPECT experimental setup.

Experimental

Materials and apparatus

The Materials, apparatus and other characterizations are discussed in SI.

Preparation of In_2O_3

0.6020 g $In(NO_3)_3 \cdot 4H_2O$ was dissolved in 40.0 mL of secondary distilled water, and then 0.1410 g citric acid was added and stirred at 1000 rpm for 20 min at room temperature. Under vigorous stirring, the solution was adjusted to pH 4.10 with 1.0 M $NH_3 \cdot H_2O$. After stirring for another 30 min at 1000 rpm, the solution was transferred to a 100 mL autoclave and reacted in an oven at 180 °C for 24 h. The solution was naturally cooled to room temperature. Subsequently, the white $In(OH)_3$ precipitate was collected by centrifugation and washed several times alternately with 30 mL of ultrapure water and 30 mL of ethanol, and then dried in an oven at 60 °C overnight. The obtained $In(OH)_3$ solid was calcined in a constant temperature furnace at 300 °C for 2 h and then ground to obtain In_2O_3 powder.

Preparation of $AgBiS_2$ microscopic flowers

0.1670 g of $AgNO_3$, 0.3155 g of $BiCl_3$ and 0.2423 g of L-cysteine were dispersed in 40.0 mL of *N*,*N*-dimethylformamide and mixed thoroughly at 1000 rpm for 30 min. The resulting mixture was then transferred into a 50 mL autoclave and heated in an oven at 200 °C for 14 h. After the reaction was completed and the mixture had cooled to room temperature, the black precipitate was collected by centrifugation and washed alternately with 30 mL of ultrapure water and 30 mL of ethanol several times. The precipitate was then dried overnight in an oven at 60 °C and milled to obtain a black $AgBiS_2$ powder.

Preparation of $In_2O_3/AgBiS_2$ heterojunction

$In_2O_3/AgBiS_2$ heterojunctions were prepared by ultrasonic mixing method with different mass ratios. In_2O_3 with a fixed mass of 1 mg and $AgBiS_2$ at varying masses were dispersed in 1.00 mL of ultrapure water and ultrasonically (100 W power) mixed for 30 min to obtain $In_2O_3/AgBiS_2$ suspension. Unless otherwise specified, the ratio of In_2O_3 to $AgBiS_2$ about $In_2O_3/AgBiS_2$ was set at 1 : 1 by default.

Preparation of apt-cDNA/$In_2O_3/AgBiS_2$ sensor

The prepared $In_2O_3/AgBiS_2$ suspension was deposited onto FTO by drop-casting 100 μL and dried at 80 °C. The sample was then incubated with 20 μL of thioglycolic acid (TGA) for 30 min at 4 °C. Subsequently, 20 μL of a mixture of 10 mM EDC and 2 mM NHS was added and incubated at 4 °C for 1 h to obtain carboxyl-activated $In_2O_3/AgBiS_2$. Then, 40 μL of 10 pM apt-cDNA mixture was introduced to the surface and left overnight in the refrigerator. Afterward, 3% BSA solution was added and incubated for 1 h at 37 °C to block the non-specific active site. Following a rinse, 10 μL of 10 nM BPA was added dropwise and allowed to stand at room temperature for 30 minutes. Hairpin DNA strand 1(H1) and Hairpin DNA strand 2(H2) were diluted to 10 μM with TEOA buffer, and annealed in a water bath at 95 °C for 5 min. After cooling, 10 μL of H1, 10 μL of H2 and 0.5 mM 0.5 μL of hemin were dropwise added to the material and incubated at 37 °C for 2 h, and then rinsed with buffer solution. Finally, 10 μL H_2O_2 and 10 μL 4-CN were dropped onto the electrode and incubated for 30 min at room temperature.

Characterization and analysis of natural polyacryla electrophoresis

1.0 μM DNA solution (200 μL) was first well dispersed in EDTA buffer containing 12.5 mM $MgCl_2$-H_2O, and subjected to a programmed temperature gradient annealing from 95 °C to 25 °C to optimize conformational stability. Subsequently, 10 μL of this DNA solution was mixed with 2 μL of 0.6 M DNA loading buffer in a 5 : 1 ratio, and the samples were separated on a 15% polyacrylamide gel electrophoresis platform in 0.1 M TBE buffer. After electrophoretic separation (30 min) at a constant voltage of 120 V, the separated bands were finally captured and recorded by a Gel Doc XR molecular imaging system.

Construction of OPECT immunosensor

The photoelectrochemical performance tests in this study were performed using a PEC/OPECT detector (Nanjing Nanda Optical Instrument Co., Ltd, Nanjing, China), and the gate was constructed on an apt-cDNA/$In_2O_3/AgBiS_2$ composite-modified fluorine-doped tin oxide (FTO) substrate. A monochromatic LED light source (5 W) with a wavelength of 410 nm was used as the excitation light source, and the tests were carried out in 10 mM phosphate buffer solution (PBS, pH 7.4) containing 0.1 M TEOA (pH = 7.4) electrolyte, and all the electrochemical characterization experiments were carried out under the condition of zero gate pressure. All measurements were performed at room temperature (25 ± 1 °C).

Results and discussion

Material preparation and characterization

Photoactive materials are very important in manipulating transistor signals through the changes of photoelectrochemical signals of the gate electrodes. In_2O_3 and $AgBiS_2$ are synthesized separately by hydrothermal method and $In_2O_3/AgBiS_2$ heterojunction is prepared by ultrasonic method. Scanning electron microscopy (SEM) results are shown in Fig. 1. In_2O_3 exhibits an average particle size of approximately 60 nm, while $AgBiS_2$ presents a flower-like structure assembled from nanosheets with an average size of about 2.5 μm. The $In_2O_3/AgBiS_2$ heterostructure shows a morphology in which $AgBiS_2$ microflowers are loaded with In_2O_3 nanoparticles. The transmission electron microscopy (TEM) characterization and elemental mapping images of the $In_2O_3/AgBiS_2$ heterojunction nanomaterials in Fig. S1 clearly reveal the heterostructure and the uniform spatial distribution of In, O, Ag, Bi and S elements,

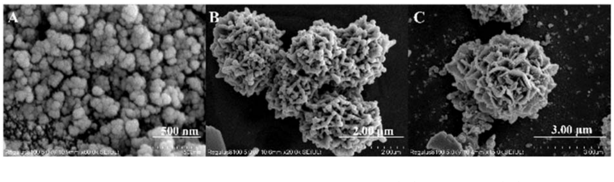

Fig. 1 Scanning electron micrographs of (A) In_2O_3. (B) $AgBiS_2$. (C) $In_2O_3/AgBiS_2$.

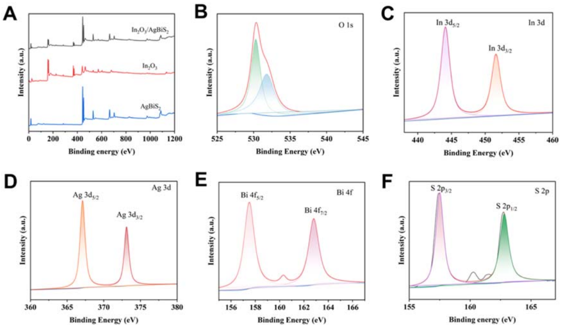

Fig. 2 XPS high-resolution spectra of (A) In_2O_3, $AgBiS_2$, $In_2O_3/AgBiS_2$. (B) O 1s. (C) In 3d. (D) Ag 3d. (E) Bi 4f and (F) S 2p.

which further verify the successful preparation of the $In_2O_3/AgBiS_2$ heterojunction nanomaterials.

As shown in Fig. 2, the XPS spectra exhibit characteristic peaks corresponding to the expected chemical states, consistent with the literature.[39] The In $3d_{5/2}$ and $3d_{3/2}$ peaks of In^{3+} appear at ~444 eV and ~452 eV, respectively. The O 1s peak (attributed to In–O bonds) is observed at ~530 eV. The Ag $3d_{5/2}$ and $3d_{3/2}$ peaks are located at ~368 eV and ~374 eV, respectively. The Bi $4f_{7/2}$ and $4f_{5/2}$ peaks of Bi^{3+} are found at ~158 eV and ~164 eV, respectively. These peak positions confirm the presence of In^{3+}, Bi^{3+} and Ag species and their corresponding chemical environments, further supporting the successful synthesis of the material.

The crystal structure of the nanomaterials was characterized by powder X-ray diffraction patterns. Fig. 3A shows the XRD patterns of In_2O_3, $AgBiS_2$ and $In_2O_3/AgBiS_2$, with the peak positions of the heterojunction corresponding to those of the two nanomaterials. The $In_2O_3/AgBiS_2$ heterojunction can be formed because of the matched band alignment between In_2O_3 and $AgBiS_2$. As depicted in Fig. 3B, the photogenerated electrons transfer from the more negative conduction band (CB) of $AgBiS_2$ to the CB of In_2O_3 and then further migrate to the FTO electrode, while the photogenerated holes migrate from the more positive valence band (VB) of In_2O_3 to the VB of $AgBiS_2$, enabling efficient spatial separation of electron–hole pairs. TEOA is oxidized to $TEOA^+$ by photogenerated holes, which quenches holes, suppresses carrier recombination and enhances the photocurrent response. To investigate the photoelectrochemical response and evaluate influence of different fabrication steps on the performance of PEC sensors, *I–t* curves of the same electrodes at various fabrication stages were recorded in 0.1 M TEOA solution in Fig. 3C. Under visible light illumination, the $In_2O_3/AgBiS_2$ composite delivers a strong current signal. Nevertheless, the current signal was drastically decreased upon the immobilization of the aptamer and its complementary strand, followed by a noticeable enhancement with the addition of BPA. Subsequently, the signal decreases significantly after the introduction of H1, H2 and hemin, which is attributed to the spatial steric hindrance effect. Finally, the dropwise addition of H_2O_2 and 4-CN triggers the generation of insoluble 4-CD precipitation, leading to a further decline in the signal. These results collectively verify the feasibility of the as-prepared photovoltaic material for biosensing applications. As charge separation efficiency is a critical factor governing the photoelectrochemical sensing performance, electrochemical impedance spectroscopy (EIS) was employed to analyze the charge transfer resistance and the separation efficiency of photogenerated electrons and holes. In general, a smaller curvature radius in the Nyquist plot indicates a lower electrochemical charge transfer resistance (R_{ct}) and higher charge transfer efficiency. The obtained Nyquist plots in Fig. 3D are consistent with the results in Fig. 3C, further corroborating the feasibility of the as-synthesized composite for photoelectrochemical sensing.

The anode signal remained reproducible over 15 repeated on/off light irradiation cycles exceeding 300 s (Fig. 4A), demonstrating the outstanding photostability of the as-fabricated sensing material. To further explore the feasibility

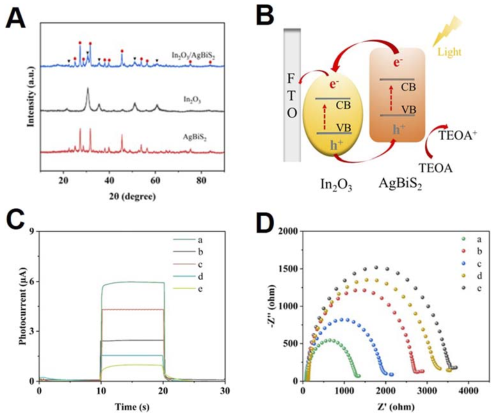

Fig. 3 (A) XRD plots of In_2O_3, $AgBiS_2$, and $In_2O_3/AgBiS_2$. (B) Charge transfer mechanism of In_2O_3 and $AgBiS_2$. (C) PEC response of (a) $In_2O_3/AgBiS_2$, (b) apt-cDNA/$In_2O_3/AgBiS_2$, (c) BPA/apt-cDNA/$In_2O_3/AgBiS_2$, (d) hemin + H1 + H2/BPA/apt-cDNA/$In_2O_3/AgBiS_2$, (e) 4-CN+H_2O_2/Hemin + H1 + H2/BPA/apt-cDNA/$In_2O_3/AgBiS_2$ (D) Nyquist plots for different sensing steps.

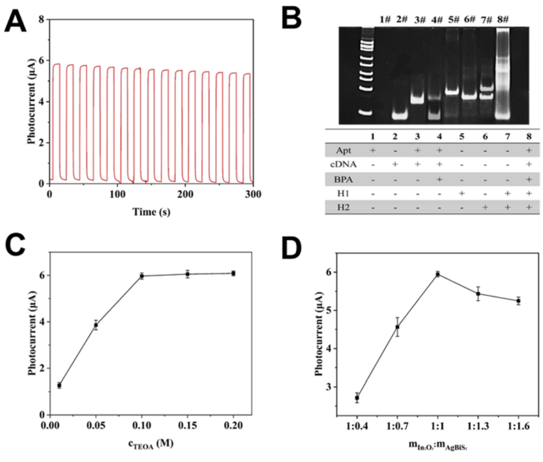

	1	2	3	4	5	6	7	8
Apt	+	-	+	+	-	-	-	+
cDNA	-	+	+	+	-	-	-	+
BPA	-	-	-	+	-	-	-	+
H1	-	-	-	-	+	-	+	+
H2	-	-	-	-	-	+	+	+

Fig. 4 (A) Stabilization of photovoltaic materials. (B) Polyacrylamide gel electrophoresis analysis. (C) Optimization of TEOA concentration. (D) Optimization of mass ratio of In_2O_3 and $AgBiS_2$.

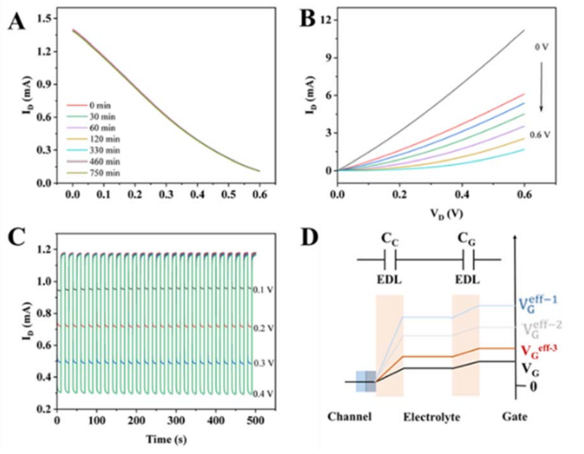

Fig. 5 (A) Transfer curve stability. (B) Output curves at different VG. (C) Potential distribution of the OPECT system upon illumination (blue line), after addition of BPA (grey line) and after addition of 4-CN and H_2O_2(red line). (D) Simulated feed voltage.

of the proposed entropy-driven amplification strategy in practical sensing context, an experimental study for the entropy-driven cycling based on BPA initiation was conducted (Fig. 4B). Specifically, polyacrylamide gel electrophoresis (PAGE) was employed to characterize the constructed entropy-driven cycling system, aiming to acquire critical insights into the physicochemical properties and operational behaviors of the sensing system and lay a solid experimental foundation for validating the efficacy of the designed entropy-driven strategy. 1#, 2#, and 3# lanes show apt, cDNA, and a double-stranded chain formed by apt and cDNA, respectively, and lane 4# is the result after the addition of BPA in the mixture of apt and cDNA. 5#, 6#, 7# and 8# show H1, H2, H1 + H2 and the lane after the completion of sensing preparation, which proves the feasibility of sensing system. Circular dichroism (CD) spectroscopy was employed to verify the formation of the G-quadruplex structure. As shown in Fig. S2, the CD spectrum of the sample with BPA exhibited a strong positive cotton effect at approximately 260–265 nm, accompanied by a negative peak near 240 nm.[51] This spectral profile is characteristic of the G-quadruplex conformation, confirming the successful folding of the DNA sequence into the desired quadruplex structure under the experimental conditions. Fig. 4C and D demonstrate the optimization of the experimental conditions, from which it can be seen that 0.1 M of TEOA is the optimal concentration, while 1 : 1 is the best mass ratio of the two single materials. The performance across a pH range of 5.0–9.0 were evaluated, which is typical for many environmental and biological matrices. The results in Fig. S3 show that the sensor exhibits optimal response at pH 7.4.

Multiple enhancement operation of OPECT

In this study, a PEDOT:PSS device with optimal performance based on the established methodology was successfully fabricated (Fig. S4). Subsequently, comprehensive characterization of the performance and stability of the organic electrochemical transistor (OPECT) based on this device was conducted. The prepared PEDOT:PSS channel was systematically tested with Ag/AgCl serving as the gate electrode.

To evaluate the long-term stability of the channel, transfer characteristics were recorded at key time points: 30, 60, 120, 330, 460, and 750 min. The overlapping curves shown in Fig. 5A indicate that the fabricated device exhibits excellent stability and maintains consistent performance over time. In addition to the transfer characteristics, the output characteristics of the device were also measured, and the results were recorded in Fig. 5B. The I_D–V_D characteristic curves measured at different gate voltages (V_G) show that the drain current (I_D) increases as the drain voltage (V_D) rises from 0 to 0.6 V. However, a higher V_G suppresses I_D to lower levels. To more comprehensively evaluate the device's response to gate voltage modulation, the dynamic response of I_D to a specific pulsed V_G step over 25 cycles was recorded, as shown in Fig. 5C. Throughout the experiment, the variation of I_D during each cycle was closely monitored. Notably, I_D consistently exhibits a fast and stable response to the specific pulse V_G over the 25 cycles. This excellent performance further demonstrates the device's sensitivity to V_G – dependent modulation and reaffirms its remarkable stability. To gain deeper insight into the physical properties and electrical behaviors of the two interfacial electric double layers (EDLs), the two interfacial double layers are modeled as two series-connected capacitors which could be seen in Fig. 5D. One of these two capacitors corresponds to C_{G-E} and the other to C_{C-E}. Fig. 5D shows that, in the presence of light, a significant photovoltage V_P is generated due to the pristine $In_2O_3/AgBiS_2$, leading to a significant increase of V_G to V_G^{eff-1}. The addition of the aptamer and its complementary chain hinders the electron transfer at the electrode surface. This inhibition is partially restored upon the addition of BPA, though the photocurrent

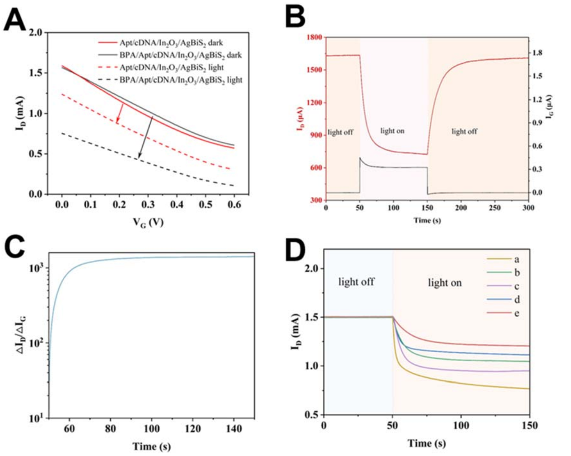

Fig. 6 (A) Transfer characteristics before and after illumination. (B) Transient response of I_G (black curve) and I_D (red curve) of the device. (C) Corresponding current gain. (D) I_D response corresponding to stepwise modification (a) $In_2O_3/AgBiS_2$, (b) apt-cDNA/$In_2O_3/AgBiS_2$, (c) BPA/apt-cDNA/$In_2O_3/AgBiS_2$, (d) Hemin + H1 + H2/BPA/apt-cDNA/$In_2O_3/AgBiS_2$, (e) 4-CN + H_2O_2/Hemin + H1 + H2/BPA/apt-cDNA-apt/$In_2O_3/AgBiS_2$.

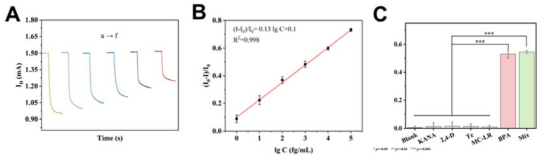

Fig. 7 (A) I_D responses to BPA with different concentrations. (B) The corresponding derived calibration curve (error bar, $n = 3$). (C) Corresponding histogram for the selectivity test. Response of the developed sensor to blank buffer, KANA, 2, 4-D, Te, MC-LR, BPA, and their mixtures. RSD values were obtained from three replicate experiments. $n = 3$. $***p \leq 0.001$.

Table 1 The recovery measurement of BPA in the real environmental water samples ($n = 3$)

Sample	Added (pg mL^{-1})	Found (pg mL^{-1}) (mean ± SD)	Recovery (%)
1	10	10.74 ± 2.76	107. 40
2	100	98.20 ± 3.54	98.20
3	1000	996.18 ± 3.89	99.62

remains lower than that of the bare heterojunction, which is named as $V_G^{\text{eff}-2}$. Upon the addition of 4-CN and H_2O_2, the precipitation reaction involving the G-quadruplex/hemin complex, 4-CN and H_2O_2 further reduces the photoelectric conversion efficiency at the electrode surface under illumination, accompanied by a reduction in gate voltage from $V_G^{\text{eff}-2}$ to $V_G^{\text{eff}-3}$.

In order to evaluate the feasibility of this scheme in the OPECT system, the transfer curves under intermittent light illumination before and after the addition of the target were systematically measured. As shown in Fig. 6A, the initial transfer characteristic curves of apt/cDNA/In_2O_3/$AgBiS_2$ exhibit a specific trend prior to BPA addition. Apt-cDNA/In_2O_3/$AgBiS_2$ (red solid curve) and apt-cDNA/In_2O_3/$AgBiS_2$/BPA (black solid curve) exhibited nearly identical transfer curves with the absence of light illumination. However, after the addition of BPA upon light illumination, the corresponding transfer curves show obvious differences before (black solid line) and after light illumination (black dashed line). As shown in Fig. 6B, in the absence of light and at $V_G = 0$, neither I_G nor I_D exhibits a significant signal changes. Upon illumination, I_G surges instantaneously and then stabilizes at approximately 0.3 μA. I_D drops sharply and stabilizes at approximately 750 μA. The current gain of the system is calculated to exceed 1000-fold (Fig. 6C), indicating that the In_2O_3/$AgBiS_2$ electrodes can effectively modulate the electrical properties of the conductive polymer poly(3,4-ethylenedioxythiophene):poly(styrene sulfonate) (PEDOT:PSS) in the channel, which provides strong support for subsequent research and applications based on this system. Fig. 6D illustrates the stepwise fabrication of the heterojunction and the corresponding I_D signal changes at each step of the OPECT sensing system, further demonstrating the feasibility of the organic photoelectrochemical transistor sensing process. All the I_D variations induced by stepwise modifications on the gate electrode in the OPECT system are recorded in Fig. 6D, which further confirms the feasibility of this organic photoelectrochemical transistor sensing platform.

Application of the OPECT detection

Since the I_D response is highly dependent on the concentration of BPA, quantitative detection can be achieved by monitoring I_D. As shown in Fig. 7A, increasing BPA concentration leads to a decrease in I_D. Fig. 7B illustrates the linear relationship between BPA concentration and normalized current response $(I_0 - I)/I_0$ variations over the range of 1 fg mL^{-1} to 0.1 ng mL^{-1}. The regression equation for the calibration curve is $(I_0 - I)/I_0 = 0.13 \lg C + 0.1$ ($R^2 = 0.998$), with the limit of detection is 0.29 fg mL^{-1}. Compared with other BPA assays summarized in Table S1, this method exhibits superior performance in terms of both linear range and detection limit.[52–55] Finally, selectivity was evaluated using potential interfering marine pollutants such as KANA, 2, 4-D, Tc, and others (Fig. 7C). Significant signal changes are observed only for the target BPA and its mixture, demonstrating the high selectivity of this sensing platform. The recognition mechanism of aptamers determines that substances with similar chemical structures exhibit comparable binding behaviors. Therefore, this method uses bisphenol A as a representative target for the detection of bisphenol compounds. In practical scenarios, the overall adverse effects and detection significance mainly stem from bisphenol analogs represented by bisphenol A.

Fig. S5 shows the variation of channel current for the same gate electrode over 6 days, indicating that apt-cDNA/In_2O_3/$AgBiS_2$ exhibits good long-term stability and reproducibility as a gate electrode for BPA detection. The current responses of different apt-cDNA/In_2O_3/$AgBiS_2$ electrode sheets toward the same analyte concentration are presented in Fig. S6, with minimal signal variation observed between electrodes. Environmental water samples were collected and diluted 1000-fold with distilled water, centrifuged and filtered through a 0.22 μm membrane, followed by BPA detection using the standard addition method. The recoveries of BPA in the water samples (Table 1) ranged from 98.20% to 107.40%, demonstrating the practical applicability of this method in real-world environments.

Conclusions

In this study, we fabricated a novel organic photoelectrochemical transistor (OPECT) incorporating an In_2O_3/$AgBiS_2$ heterojunction as the gate electrode, enabling sensitive BPA detection *via* the coupled mechanisms of biocatalytic precipitation and hybridization chain amplification. Under optimized conditions, the sensor demonstrates a broad linear range, high sensitivity, exceptional selectivity, and promising applicability for BPA quantification in complex environmental matrices. The signal amplification strategy presented herein offers a valuable paradigm for the development of advanced sensing platforms targeting marine pollutants.

Conflicts of interest

There are no conflicts to declare.

Data availability

The data supporting this article have been included as part of the supplementary information (SI). Supplementary information is available. See DOI: https://doi.org/10.1039/d6ra02509a.

Acknowledgements

This work was financially supported by the National Natural Science Foundation of China (22104042), the Open Fund of the Key Laboratory of Optoelectronic Sensing and Life Analysis, Ministry of Education, Qingdao University of Science and Technology (OES-2025-04) and the Natural Science Foundation of Huaian (HAB202232).

References

1 H. Tao, F. Xie, Z. Li, L. Qu, Q. Zha and M. Zhu, *RSC Adv.*, 2025, **15**, 26039–26047.

2 G. A. Idowu, T. L. David and A. M. Idowu, *Mar. Pollut. Bull.*, 2022, **176**, 113444.

3 H. Sambe, K. Hoshina, K. Hosoya and J. Haginaka, *J. Chromatogr. A*, 2006, **1134**, 16–23.

4 Y. Mutou, Y. Ibuki, Y. Terao, S. Kojima and R. Goto, *Environ. Toxicol. Pharmacol.*, 2006, **21**, 283–289.

5 P. Y. Sun and Y. H. Wu, *Sens. Actuators B Chem.*, 2013, **178**, 113–118.

6 F. C. Moraes, I. Cesarino, V. Cesarino, L. H. Mascaro and S. A. S. Machado, *Electrochim. Acta*, 2012, **85**, 560–565.

7 Q. Liu, X. Z. Kang, L. Z. Xing, Z. X. Ye and Y. C. Yang, *RSC Adv.*, 2020, **10**, 6156–6162.

8 D. D. Seachrist, K. W. Bonk, S. M. Ho, G. S. Prins, A. M. Soto and R. A. Keri, *Reprod. Toxicol.*, 2016, **59**, 167–182.

9 J. R. Rochester, *Reprod. Toxicol.*, 2013, **42**, 132–155.

10 A. E. Peters, E. A. Ford, S. D. Roman, E. G. Bromfield, B. Nixon, K. G. Pringle and J. M. Sutherland, *Hum. Reprod. Update*, 2024, **30**, 653–691.

11 P. A. Fowler, M. Bellingham, K. D. Sinclair, N. P. Evans, P. Pocar, B. Fischer, K. Schaedlich, J. S. Schmidt, M. R. Amezaga, S. Bhattacharya, S. M. Rhind and P. J. O'Shaughnessy, *Mol. Cell. Endocrinol.*, 2012, **355**, 231–239.

12 J. Wang, Y. Pan, L. Jiang, M. Liu, F. Liu, M. Jia, J. Li and Y. Lai, *ACS Appl. Mater. Interfaces*, 2019, **11**, 37541–37549.

13 W. W. Zhao, J. J. Xu and H. Y. Chen, *Chem. Soc. Rev.*, 2015, **44**, 729–741.

14 H. Y. Wang, M. D. Xu, D. Wu, D. Y. Tie, M. J. Li and D. P. Tang, *Anal. Chem.*, 2026, **98**, 7114–7122.

15 J. Qin, D. Wu, Z. C. Yu and D. P. Tang, *Anal. Chem.*, 2025, **97**, 23631–23639.

16 D. Ohayon, V. Druet and S. Inal, *Chem. Soc. Rev.*, 2023, **52**, 1001–1023.

17 J. Rivnay, S. Inal, A. Salleo, R. M. Owens, M. Berggren and G. G. Malliaras, *Nat. Rev. Mater.*, 2018, **3**, 17086.

18 U. Boda, I. Petsagkourakis, V. Beni, P. A. Ersman and K. Tybrandt, *Adv. Mater. Technol.*, 2023, **8**, 2300247.

19 J. Kawahara, P. A. Ersman, K. Katoh and M. Berggren, *IEEE T. Electron Dev.*, 2013, **60**, 2052–2056.

20 P. A. Ersman, D. Nilsson, J. Kawahara, G. Gustafsson and M. Berggren, *Org. Electron.*, 2013, **14**, 1276–1280.

21 D. A. Koutsouras, M. H. Amiri, P. W. M. Blom, F. Torricelli, K. Asadi and P. Gkoupidenis, *Adv. Funct. Mater.*, 2021, **31**, 2011013.

22 M. Moser, J. F. Ponder, A. Wadsworth, A. Giovannitti and I. McCulloch, *Adv. Funct. Mater.*, 2018, **29**, 1807033.

23 J. M. Zhang, Y. Gao, Y. C. Zhu, R. Ban, Y. M. Li, H. Du, F. Z. Chen and W. W. Zhao, *Anal. Chem.*, 2025, **97**, 4365–4372.

24 T. Cai, W. R. Zhang, L. Z. Lian, Y. L. Sun, Z. H. Xia, Y. X. Chen, J. Shuai, P. Lin, Q. Zhang and S. H. Liu, *Anal. Chem.*, 2025, **97**, 526–534.

25 T. M. Li, Z. Qu, J. S. Si, Y. Lee, V. K. Bandari and O. G. Schmidt, *Sci. Adv.*, 2025, **11**, eadt5186.

26 C. Yuan, K. X. Xu, Y. T. Huang, J. J. Xu and W. W. Zhao, *Adv. Mater.*, 2024, **36**, 2407654.

27 H. H. Cai, X. H. Zhang, L. Zhang, C. Luo, H. J. Lin, D. M. Han, F. Z. Chen and C. Huang, *Anal. Chem.*, 2024, **96**, 12739–12747.

28 J. Y. Tang, J. Y. Pang, X. X. Lv and X. L. Wang, *ACS Appl. Energy Mater.*, 2025, **8**, 9683–9690.

29 P. Lu, K. Liu, Y. Liu, Z. L. Ji, X. X. Wang, B. Hui, Y. K. Zhu, D. J. Yang and L. H. Jiang, *Appl. Catal. B: Environ. Energy*, 2024, **345**, 123697.

30 X. Huang, Q. Y. Lin, L. L. Lu, M. J. Li and D. P. Tang, *Anal. Chim., Acta*, 2022, **1228**, 340358.

31 R. J. Zeng, L. J. Zhang, Z. B. Luo and D. P. Tang, *Anal. Chem.*, 2019, **91**, 7835–7841.

32 S. X. Tang, X. F. Luo, Q. M. Chen, Y. Du, C. Q. Zhang and X. Y. Zhang, *J. Alloy. Compd.*, 2025, **1026**, 180513.

33 J. M. Tian, X. Chen, T. Q. Wang, W. Y. Pei, F. Li, D. Li, Y. Yang and X. T. Dong, *Sens. Actuators B Chem.*, 2021, **344**, 130227.

34 D. L. Kong, B. Hong, J. C. Xu, X. L. Peng, J. Li, H. W. Chen, S. iu, N. Zhang and X. Q. Wang, *Appl. Surf. Sci.*, 2025, **688**, 162442.

35 Z. Y. Yuan, N. H. Chu and F. L. Meng, *Sens. Actuators B Chem.*, 2024, **406**, 135415.

36 P. Chang, Y. H. Wang, Y. T. Wang and Y. Y. Zhu, *Chem. Eng. J.*, 2022, **450**, 137804.

37 Y. R. Wang, Q. X. Zhong, R. Zhu and L. C. Zhao, *J. Energy Chem.*, 2026, **114**, 868–885.

38 W. Z. Wang, S. R. Bao, C. X. Gao, T. C. Huang, Y. Zhu and R. Xu, *Mat. Sci. Eng. B*, 2024, **310**, 117739.

39 L. Li, C. L. S, J. H. Li, J. L. Liu, Y. L. Li and Q. J. Xie, *Mikrochim. Acta*, 2023, **190**, 192.

40 R. J. Zeng, H. X. Gong, Y. L. Li, Y. X. Li, W. Lin, D. P. Tang and D. Knopp, *Anal. Chem.*, 2022, **94**, 7442–7448.

41 K. Y. Zhang, S. Z. Lv, Z. Z. Lin, M. J. Li and D. P. Tang, *Biosens. Bioelectron.*, 2018, **101**, 159–166.

42 D. Wu, Z. C. Yu, J. Qin, M. J. Li and D. P. Tang, *Anal. Chem.*, 2025, **97**, 10947–10954.

43 Y. S. Wang, S. Tian, S. Y. Chen, M. J. Li and D. P. Tang, *Anal. Chem.*, 2025, **97**, 7526–7535.

44 G. C. Han, X. Z. Feng and Z. C. Chen, *Int. J. Electrochem. Sci.*, 2015, **10**, 3897–3913.

45 X. Zhu, L. Gao, L. Tang, B. Peng, H. Huang, J. Wang, J. Yu, X. Ouyang and J. Tan, *Biosens. Bioelectron.*, 2019, **146**, 111756.

46 A. Qileng, J. Wei, N. Lu, W. Liu, Y. Cai, M. Chen, H. Lei and Y. Liu, *Biosens. Bioelectron.*, 2018, **106**, 219–226.

47 E. H. Lee, H. J. Lim, S. D. Lee and A. Son, *ACS Appl. Mater. Interfaces*, 2017, **9**, 14889–14898.

48 M. Jo, J. Ahn, J. Lee, S. Lee, S. Hong, J. Yoo, J. Kang, P. Dua, D. Lee, S. Hong and S. Kim, *Oligonucleotides*, 2011, **21**, 85–91.

49 M. E. Schiano, A. Abduvakhidov, M. Varra and S. Albrizio, *Appl. Sci.*, 2022, **12**, 3752.

50 Y. Wu, I. Belmonte, K. S. Sykes, Y. Xiao and R. J. White, *Anal. Chem.*, 2019, **91**, 15335–15344.

51 X. J. Yang, L. Q Yuan, Y. Xu and B. F. He, *Anal. Chim. Acta*, 2023, **1247**, 340879.

52 W. W. Sun, Y. F. Qi, L. Wang, Y. P. Tan, X. Zhang, J. F. Wang and Y. B. Li, *Spectrochim. Acta A Mol. Biomol. Spectrosc.*, 2025, **327**, 125318.

53 W. Liu, M. Y. Li, P. L. Zhang, H. M. Jiang, W. J. Liu, J. Y. Guan, Y. H. Sun, X. Y. Liu and Q. Zeng, *Mikrochim. Acta*, 2024, **191**, 309.

54 Y. Zhang, W. Zhang, L. Zhang, G. Song, N. Wang, W. Xu and W. Huang, *Microchem. J.*, 2021, **170**, 106737.

55 J. J. Feng, L. G. Xu, G. Cui, X. L. Wu, W. Ma, H. Kuang and C. L. Xu, *Biosens. Bioelectron.*, 2016, **81**, 138–142.